Journal of Materials Chemistry A

Degradation mechanisms in mixed-cation and mixed-halide $Cs_xFA_{1-x}Pb(Br_yI_{1-y})_3$ perovskite films under ambient conditions

Journal:	*Journal of Materials Chemistry A*
Manuscript ID	TA-ART-01-2020-001201.R3
Article Type:	Paper
Date Submitted by the Author:	15-Apr-2020
Complete List of Authors:	Marchezi, Paulo; Universidade Estadual de Campinas, Chemistry Institute Therézio, Eralci; Universidade Federal de Mato Grosso, Physics Institute; UNICAMP, Chemistry Institute Szostak, Rodrigo; State University of Campinas, ; Laboratório Nacional de Luz Síncrotron, Loureiro, Hugo; UNICAMP, Chemistry Institute Brüning, Karsten; SLAC National Accelerator Laboratory, Materials Science Division Gold-Parker, Aryeh; Stanford University, Chemistry; Stanford Synchrotron Radiation Lightsource Melo Jr, Mauricio; University of Sao Paulo, São Carlos Institute of Physics Tassone, Christopher; Stanford Synchrotron Radiation Lightsource, Materials Science Tolentino, Hélio; Laboratório Nacional de Luz Síncrotron, Toney, Michael; Stanford Synchrotron Radiation Laboratory, Nogueira, Ana Flavia; Universidade Estadual de Campinas, Instituto de Quimica

ARTICLE

Degradation mechanisms in mixed-cation and mixed-halide $Cs_xFA_{1-x}Pb(Br_yI_{1-y})_3$ perovskite films under ambient conditions

Received 00th January 20xx,
Accepted 00th January 20xx

DOI: 10.1039/x0xx00000x

Paulo Ernesto Marchezi[a], Eralci Moreira Therézio[a,b], Rodrigo Szostak[a], Hugo Campos Loureiro[a], Karsten Bruening[c], Aryeh Gold-Parker[c], Maurício A. Melo Jr.[d], Christopher J. Tassone[c], Helio C. N. Tolentino[e], Michael F. Toney[c] and Ana Flávia Nogueira*[a]

Multicomponent perovskites of the type $Cs_xFA_{1-x}Pb(Br_yI_{1-y})_3$ are good candidates for high efficient perovskite and tandem solar cells. In this work the degradation mechanims of these multicomponent films were investigated and our results show that the degradation is a complex process, with the formation of a number of intermediates and lead-based products. *In-situ* X-ray diffraction analysis carried out in the first stages of the degradation indicate that differently from $MAPbI_3$ perovskite, the degradation of these multicomponent films begins with the formation of hexagonal polytypes as intermediates, which in turn are converted to hydrated phases. The initial steps of the degradation were also monitored for the first time by *in-situ* environmental scanning electron microscopy (ESEM) with 75% of relative humidity. *In-situ* ESEM images show that the degradation has its beginning at the "valleys" of the wrinkled morphology found in these films, possibly because of smaller grain size in these regions. XPS analysis confirm that the hydrated perovskite films continue to react with the environment, leading to the formation of metal hydroxide, carbonate, and oxide as final products. Our results also indicate that the degradation mechanism are highly dependent on the Cs concentration and Br content providing a guide for choosing the best compositions for efficient, but more environmentally stable solar cells.

Introduction

In the last decade, the research on organic-inorganic, hybrid perovskite solar cells (PSC) has advanced rapidly due to their excellent optoelectronic properties combined with low-cost and solution-process fabrication methods. These materials present tailorable bandgap, ambipolar charge transport, long diffusion length of the charge carriers, and high defect tolerance, which make them very attractive for efficient photovoltaic solar cells.[1–6] PSC have recently achieved an impressive power conversion efficiency (PCE) of 25.2%,[8] attracting much interest from the industry to manufacture large area modules and tandem devices.[9–11]

The light-harvesting perovskite material, with chemical formula ABX_3, commonly refers to a 3D organic-inorganic, hybrid compound in which A is a monovalent cation such as methylammonium (MA, $CH_3NH_3^+$), formamidinium (FA, $CH(NH_2)_2^+$), or Caesium (Cs^+); B is a divalent metal such as lead (Pb^{2+}) or tin (Sn^{2+}); and X is a halide anion, as bromide (Br^-) or iodide (I^-). It is possible to combine cations (*e.g.,* adding Cs^+ into $FAPbI_3$ or replacing Pb^{2+} with Sn^{2+}) or anions (*e.g.*, mixing Br^- and I^-) in the crystal lattice. Due to this composition flexibility, one can tune the bandgap (E_g), making them suitable to single junction solar cells (1.1 – 1.4 eV) or tandem solar cells (where this material is applied as a top semiconducting layer).[12–14] The interest in tandem solar cells (all perovskite, Si-perovskite, CIGS-perovskite) is due to the possibility to overcome the Shockley-Queisser limit for single layer cells.[15–17] As an example, $Cs_xFA_{1-x}Pb(Br_yI_{1-y})_3$ and $MA_yFA_{1-y}Pb(Br_yI_{1-y})_3$ compositions are appealing because of their adjustable bandgap by mixing Cs, MA and FA at the A-site and Br^- and I^- at X-site.[18,19]

To make possible large-scale application, it is essential to control the H_2O permeation to prevent perovskite degradation. The long-term stability of perovskite solar cells is generally achieved by incorporating H_2O barrier layers on the back side of the device. Nevertheless, for solar cells with physical encapsulation, lower PCEs have been reported and further improvement is necessary and intrinsic stability is highly desierable.[20–24] The knowledge and control of the intermediates and final products formed during degradation is crucial to propose new strategies to decrease degradation. There are many reports concerning the degradation of $MAPbI_3$ and $MAPbBr_3$ films.[25–32] A common agreement in the literature is that water plays a catalytic role in the entire degradation process, and PbX_2 is the major degradation product. Many degradation routes have been proposed with different intermediates and final products, which, we believe, is a consequence of the diverse conditions that the films are

[a] Chemistry Institute, University of Campinas, Campinas, SP, Brazil.
[b] Physics Institute, Federal University of Mato Grosso, Cuiabá, MT, Brazil.
[c] Stanford Synchrotron Radiation LightSource (SSRL), Menlo Park, California, USA.
[d] São Carlos Institute of Physics, University of São Paulo, 13560-970, São Carlos, SP, Brazil.
[e] Brazilian Synchrotron Light Laboratory (LNLS), Brazilian Center for Research in Energy and Materials (CNPEM), Campinas, SP 13083-970, Brazil.

allowed to degrade.[30] Nevertheless, there is still little knowledge regarding the degradation of mixed cations, mixed halide perovskites ($Cs_xFA_{1-x}Pb(Br_yI_{1-y})_3$).[31]

In this work, we describe a systematic investigation of the degradation mechanism in mixed-halide, mixed-cation perovskites ($Cs_xFA_{1-x}Pb(Br_yI_{1-y})_3$, where x = 0.10, 0.17 and 0.20 and y = 0.17 and 0.38. These multicomponent films were allowed to degrade in ambient conditions for 60 days and both morphology and changes in their chemical composition were evaluated by X-ray photoelectron spectroscopy (XPS), *in-situ* scanning electron microscopy (SEM), and *in-situ* X-ray diffraction (XRD) studies. Our results show that the degradation is influenced by the fraction of bromide and caesium. Furthermore, the degradation of multicomponent perovskite not only converts the perovskite to its precursor materials, but the degradation process passes through several intermediate phases, beginning with transitions into hexagonal perovskite phases prior to hydrated phases. These pathways are different from $MAPbX_3$. Further hydration of these phases results in the formation of many compounds such as oxides and carbonates.

Experimental

Precursor solutions

To prepare the precursor solutions, the following chemicals were purchased from Sigma-Aldrich: formamidinium iodide (FAI, >98%), caesium iodide (CsI, 99.99%), lead bromide ($PbBr_2$, >98%) and lead iodide (PbI_2, 99%), which were dissolved in 1M solution of N,N-dimethylformamide (DMF) and dimethyl sulfoxide (DMSO) (4:1 DMF:DMSO). The precursor solutions were prepared according to the following composition: $Cs_xFA_{1-x}Pb(Br_yI_{1-y})_3$, where x = 0.10, 0.17 or 0.20 and y = 0.17 or 0.38. The films were named depending on the composition (x/y) as follows: 10/17, 17/17, 20/17, 10/38, 17/38 and 20/38.

Film deposition

Glass substrates were soaked in a *piranha* solution (five parts of concentrated H_2SO_4 and two parts of H_2O_2 (30%)) for 10 minutes, and then rinsed, first in water, then in isopropanol and dried under N_2 flow. The perovskite films were then deposited using the solvent engineering method,[33] following a two steps procedure: 10 s at 1000 rpm and 30 s at 6000 rpm, through spin-coating. The anti-solvent (chlorobenzene) was dropped on the spinning substrate 10 s before the end of the spinning. The films were then annealed at 100 °C for 30 min, in a N_2 glove box.

Characterization

In-situ GIWAXS measurements were performed in the XRD2 beam line at the National Synchrotron Light Laboratory (LNLS), Campinas, Brazil. The samples were transferred from inert atmosphere into the GIWAXS chamber. The samples were, then, measured at 0% relative humidity (RH). After 10 min, the chamber was filled with moisture until reach 40% RH. The X-ray scattering was collected for 60 min in this RH, then the RH was increased to 60%. Again, the samples were measured for 60 min. After that, the RH was turned back to 0% and the scattering was measured for 60 min. The X-ray energy was 7 kV and the scattering signal was collected by a Dectris Pilatus 300k detector with integration time of 1 s, placed at 190.47 mm from the sample. The angle of incidence of the X-ray beam was set to 3° with exposure time of 5 s and sleep time of 25 s. Each GIWAXS image was calibrated using AgBE standard and azimuthally integrated between 270-50° to obtain 1D X-ray diffraction patterns using the *fit2D* software package. *Ex-situ* GIWAXS was performed at the 11-3 beamline at the Stanford Synchrotron Radiation Lightsource (SSRL) with a photon energy of 12.7 keV, using a Rayonix MX225 CCD detector. The sample was placed in helium atmosphere during GIWAXS acquisition. Images were calibrated using LaB6 and integrated azimuthally, in a range of 30-150°, to get 1D patterns using the Nika software package. The reciprocal lattice maps were calculated using pigyx and py-FAI python libraries.

The morphology of perovskite films was investigated through scanning electron microscopy using a Quanta 250 microscope coupled with a field emission-scanning (FEG-SEM) in which, concomitantly, dispersive energy spectroscopy (EDS) was performed on the top of the perovskite film. *In-situ* FEG-SEM was performed in environmental mode (FEG-ESEM), maintaining the films inside the microscope chamber at 75% of RH for 5 h.

UV-Vis absorption spectra were obtained with an Agilent Cary 60 Absorption Spectrophotometer by transmitting an open beam of polychromatic light from a Deuterium-Tungsten light source (DH-2000-BAL), operating in the range of 215 nm to 2500 nm.

Perovskite surface composition was also studied using X-ray photoelectron spectroscopy (XPS) under a reduced pressure of 10^{-9} Pa with a Scient Omicron ESCA+ spectrometer containing a high-performance hemispheric analyser (EA-125). Monochromatic Al Kα (1486.6 eV) was employed as the excitation source. The data analysis was performed in CasaXPS, setting the C 1s peak at 284.8 eV as the reference for calibration.

Results and discussion

The classical ABX_3 perovskite structure shows various polytypes depending on the stacking sequence of the close-packed AX_3 layers.[34] In this work, we use the well-established Ramsdell notation[35] to refer to the phases observed in the degradation process, as reported previously in the literature.[36] For example, the photoactive α phase is composed of cubic closed-packed AX_3 layers, resulting in a 3D framework of BX_6 corner-sharing octahedral (3C phase). Moreover, the yellow δ phase already observed in lead halide perovskites is composed of pure hexagonal closed-packed AX_3 phase (2H phase). The other two common intermediate phases are composed of a combination of hexagonal and cubic phases (4H and 6H phases), resulting in a 3D framework of both face-sharing and corner-sharing BX_6 octahedra.[34,37]

In order to study the initial stages of degradation in multicomponent perovskite films, *in-situ* grazing incidence wide angle X-ray scattering (GIWAXS) was carried out at different RH conditions (setup in Figure 1a). For this study, the compositions 10/17, 20/17, 10/38 and 20/38 were chosen. Figure 1b shows the XRD patterns of the fresh samples which exhibit the main perovskite diffraction peaks.

For the fresh samples, the diffraction peaks assigned to orthorhombic $CsPb(I_xBr_{1-x})_3$ phase at q ~7 nm^{-1} are observed for the 20/17 and 20/38 compositions only (Figure 1d and f). This could be related to the lower solubility of Cs in the precursor solution.[38] However, for the 20/17 the intensity of this peak increases up to 60% RH while for the 20/38 the intensity remains constant. Due to the small amount of Cs in the 10/17 sample, this peak appears only at 60% RH and its intensity increases continuously. Interestingly, this peak does not appear for the 10/38 sample in any conditions (Figure 1e). The formation of $CsPb(I_xBr_{1-x})_3$ is an irreversible process which is evident when the samples are set back again to 0% RH. After one hour at 60% RH, all samples exhibit peaks related to hexagonal phases. Sample 10/17 shows the 4H (q = 8.3 and 9.6 nm^{-1}) and 2H (q = 8.4 nm^{-1}) hexagonal phases, while sample 20/17 presents only a small signal related to the 4H phase (Figure 1c and d). For the samples with 38% Br, the formation of intermediates is different. For the sample 20/38 we observe the formation of both hexagonal 6H phases (q ~8.8 nm^{-1}) and hydrated perovskite (q ~8.0 nm^{-1}) simultaneously, independent of the environment. For the 10/38, the hydrated perovskite appears only at 60% RH. We conclude that Cs and Br contents drive the formation of a certain type of hexagonal phase with concomitant formation (or not) of hydrated perovskite.

In addition, we observe an increase in the intensity of the peaks related to the hexagonal phases for all samples except the film with composition 20/17 (Figure 1c-f), which is our most stable sample. Another important conclusion here is that

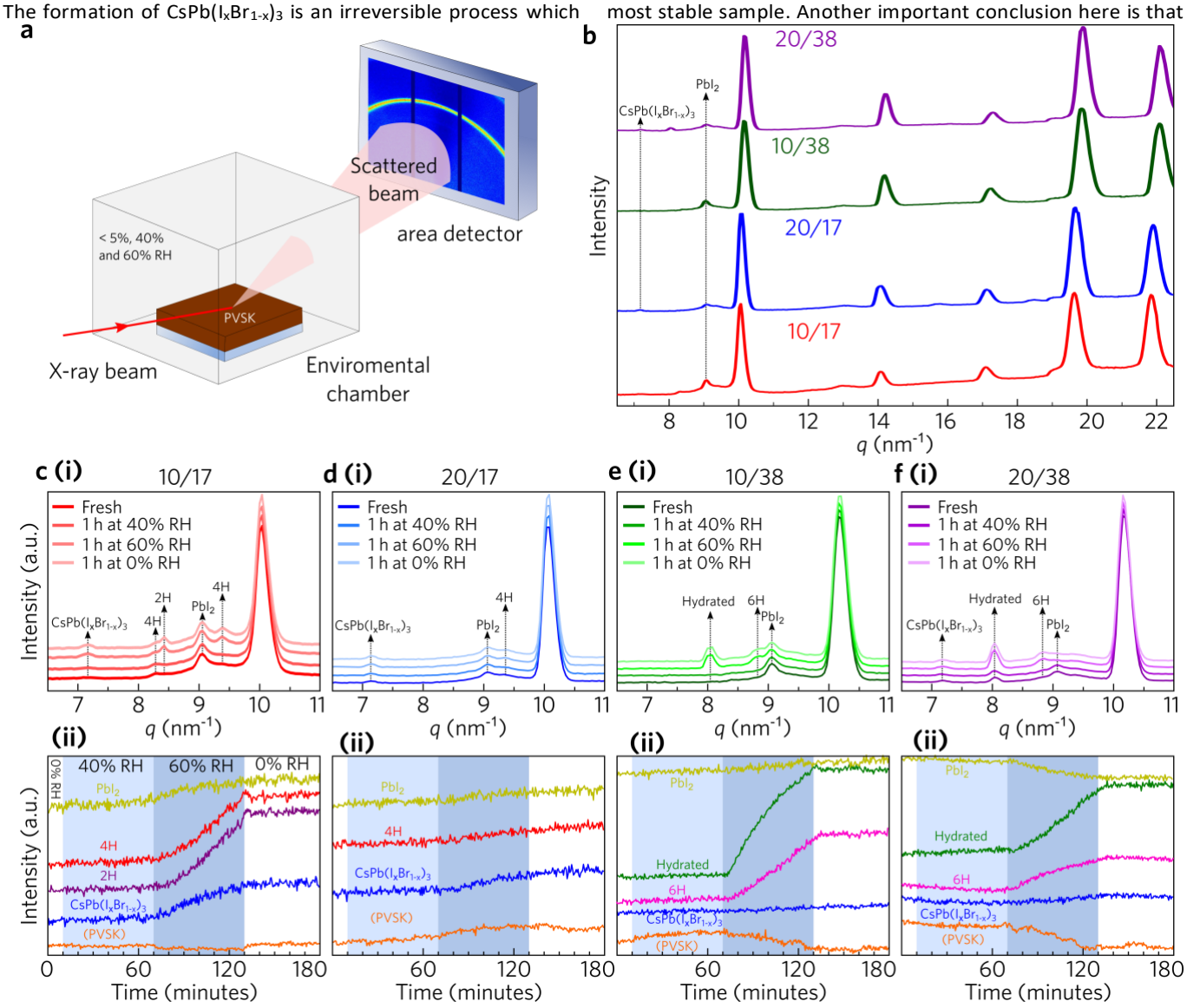

Figure 1: *In-situ* GIWAXS measurements at different RH conditions. (a) Scheme of the experimental apparatus. (b) XRD patterns of the fresh samples. (c-f) XRD patterns for all samples at different RH conditions. (ii) Evolution in intensity of selected peaks of $CsPb(I_xBr_{1-x})_3$, 2H, 4H, 6H, PbI_2 and hydrated perovskite, as a function of time. The reciprocal lattice maps for all the 1D profiles are presented in Figures S1 – S4.

the increase of Cs yields more water-tolerant films, as observed in previous reports.[39] However, the increase in the Br content accelerates degradation, as seen by the appearance of peaks related to hydrated perovskites in the films with 38% Br (Figure 1e and 1f) in the first stages of the degradation process.

The samples were also analysed after the complete degradation. Figure 2 shows the integrated 1D profiles from ex-situ GIWAXS taken after 60 days under ambient condition. The black phase of the perovskite is, in its majority, converted into other phases and products, evidenced by the dramatic decrease in the intensity of the diffraction peak at q = 10 nm^{-1} ((100) black-phase perovskite). For all compositions, a peak at q = 7.9 nm^{-1} emerges after degradation. For methylammonium perovskite, the monohydrate product was reported to form metastable, thin, pale-yellow needles that can undergo further hydration, forming dihydrate crystals.[40–42] Hence, we attribute the peak at q = 7.9 nm^{-1} to the formation of $(Cs_xFA_{1-x})_4Pb(Br_yI_{1-y})_6{\cdot}2H_2O$. This peak is slightly shifted to lower q due to the larger size of the FA cations. Besides, these peaks are quite intense, which is characteristic of these hydrated phases. The dihydrate perovskite can be considered as a network of isolated $[PbI_6]^{4-}$ octahedra balanced by surrounding H_2O, FA^+ and Cs^+ cations.[43] Additional peaks related to perovskite degradation products were also observed. The two peaks at q = 6.9 and 7.0 nm^{-1} are the (101) and (002) peaks of orthorhombic $CsPb(I_xBr_{1-x})_3$.[44] The sample 10/38 does not present this peak and for samples 17/38 and 20/38, these peaks are shifted to higher q indicating the incorporation of more Br in the structure. The peaks at q = 8.2 and 9.1 nm^{-1}, respectively) are attributed to the 4H hexagonal phase.[36] The 4H phase is composed by I and Br and the shift of these peaks to higher q is explained by replacement of I by Br.[34] The 38% Br samples present well-defined peaks at q = 8.7 and 10.1 nm^{-1}, related to 6H perovskite polytypes (Figure 2). The hexagonal 6H phase is reported as being Br-rich phase[34], and this explains why these hexagonal phases are not found in the 17% Br series. [36] The 10/17 composition presents unique features, as can be seen by the presence of PbI_2, which is not present in the other samples. It seems that the formation of 2H phases (formed exclusively by I) in this composition in the first stages might be related to the presence of more PbI_2.[40].

In-situ and ex-situ GIWAXS results confirm that the initial stages of the degradation of multicomponent perovskites pass through the formation of the hexagonal phases prior to the hydrated phases. The exception is the 20/38 sample were both the hexagonal phase (6H) and the hydrated perovskite are found in all ambient conditions investigated. In summary, samples containing 17% of Br pass through 4H and 2H hexagonal phases prior to the degradation into hydrated phases. On the other hand, samples with 38% of Br form the phase 6H and hydrated perovskite phases almost simultaneously. It corroborates what was already reported earlier by Dang *et al.*[34], that Br-rich perovskites present heterogeneous distribution of Br^- and I^-. Thus, isolated Br-rich regions in the pristine perovskite promote the formation of 6H phase (Br-rich phase). Simultaneously, the I-rich regions become more suitable to incorporate water in the structure, leading to the formation of the hydrated perovskite. Interestingly, we have recently reported through *in-situ* GIWAXS that the initial steps in perovskite film formation also pass through the formation of hexagonal phases and intermediates; and that water content has an important role in directing the formation of these structures.[45]

For a better understanding of the initial stages of the degradation, we analyse the formation of the hexagonal and hydrate phases by subjecting the samples to *in-situ* FEG-ESEM imaging. *In-situ* FEG-ESEM images were taken during the exposure of the sample 10/17 and 10/38 to a RH of 75% for 5 hours, in order to monitor the degradation reactions (see the videos in the Supplementary Information). To our knowledge, this is the first time that *in-situ* degradation analysis through ESEM has been carried out in perovskite films. Figures 3a-g show screenshots of each hour of humidity exposure during the ESEM imaging of sample 10/17. Film wrinkling is observed in all fresh samples and it has been assigned to a mechanical stress during the formation of crystalline intermediates and their subsequent conversion to black phase perovskite.[46] Complete degradation was achieved after 5 h of exposure and

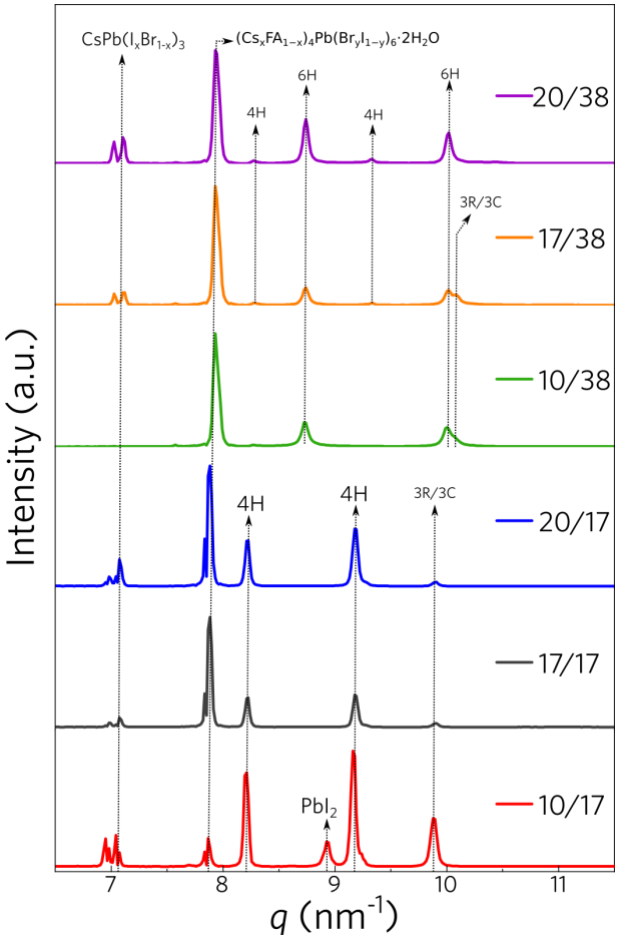

Figure 2: XRD patterns of perovskite films taken after 60 days at uncontrolled laboratory ambient conditions. All range of q analysed and the XRD pattterns taken before degradation are presented in Figure S5. The respective reciprocal lattice maps are presented in Figures S6 and S7.

it occurred mainly in the electron beam exposed area. Secondary electrons generated at the sample surface collide and ionize water molecules as they are accelerated towards a positively biased gaseous secondary electron detector. The ionization of water causes a cascade of reactions and the positively charged ions (H_xO^+) are accelerated towards the sample surface counterbalancing the charge and, in the case of perovskite samples, reacting with it, increasing the degradation rate of the area exposed to the electron beam. We saw that the degradation has its beginning in the "valleys" of the wrinkled film. We believe that this is related to the presence of smaller perovskite grains at the "valleys" compared to the "hills", as we can see in the cross-section SEM images (Figure S8). Furthermore, for sample 10/17, at about 1 hour of exposure, few grains start to coalesce (Figure 3b). We assigned these structures to the hexagonal phases (4H and 2H), corroborating with the *in-situ* GIWAXS results. After 2 hours, we observe the formation of needle-like structures (Figure 3c), previously assigned in the literature to hydrated perovskites.[31,32,43] It is important to point out that our assumptions were based on the fact that both *in situ* GiWAXS and SEM track the degradation with time. It is necessary further analyses to confirm our findings.

For sample 10/38 (Figure S9), the hydration and the hexagonal phases begin to appear almost at the same time (Figure S9 and Supporting Videos). In addition, the degradation starts faster compared to the sample 10/17. The first degradation products begin to appear 15 min after contact with humidity atmosphere (Figure S9b). In addition, the complete hydration of the perovskite occurs within 2 hours. These results agree with the *in-situ* GIWAXS data where more Br causes a much higher instability in the perovskite films. As control experiment, the same procedure but now in high-vacuum mode was carried out to avoid the influence of humidity. Figure S10 and the Supporting Videos show that the electron beam does not degrades the sample in the same way as the humidity inside the microscope chamber.

SEM images, before and after degradation, were also obtained to track the change in morphology with time. Comparing Figures S11a (fresh) and S11b (aged at ambient conditions), we observe that the morphology, shape, and contour of the grains are completely different. Besides, after degradation, there is a coalescence of the grains associated with formation of other phases and products, as expected due to the very unstable nature of the perovskite towards moisture. Samples with 17% of Br present needle-like structures. These structures have already been observed previously [30,47] and have been assigned to hydrated perovskite. We could not find any compositional inhomogeneity, on length scale of 50 µm, in the perovskite layer by Energy Dispersive Spectroscopy (EDS) (Figures S12 and S13).

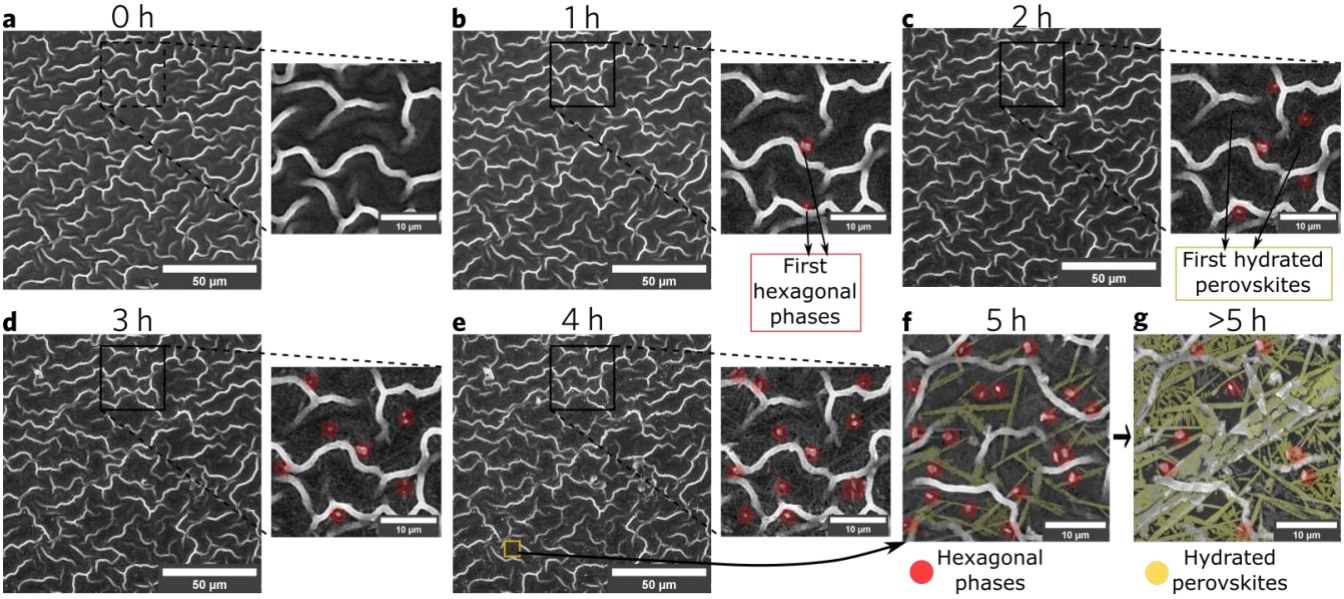

Figure 3: *In-situ* FEG-ESEM images during degradation of sample 10/ 17 upon humidity exposure (75% RH). (a) fresh sample, (b) 1h, (c) 2 h, (d) 3 h, (e) 4 h and (f-g) higher magnification to see the formaton of hydratd perovskite structures. See the Supporting Videos for a real-time visualization.

Changes in the colour and absorption profile directly confirm the decomposition of the perovskite structure after prolonged ambient exposure (Figure 4a-f). The UV-vis spectra of the fresh samples show the characteristic absorption onset at ~765 nm for 17%Br- and ~710 nm for 38%Br-based perovskites, corresponding to their optical band gap, E_g = 1.62 eV and E_g = 1.75 eV, respectively. The increase in band gap is caused by the higher content of Br and Cs in the perovskite structure.[48] We notice that a more abrupt visual change starts to appear in the second day and the films are entirely degraded after 20 days. For samples with 17% of Br, in day 2, the onset shifts to higher wavelengths and a broad absorption band appears around 550 nm, related to the presence of hexagonal phases.[36] In day 3, samples 17/17 and 20/17 present an absorption at 500 nm (4H phase) that evolves to a

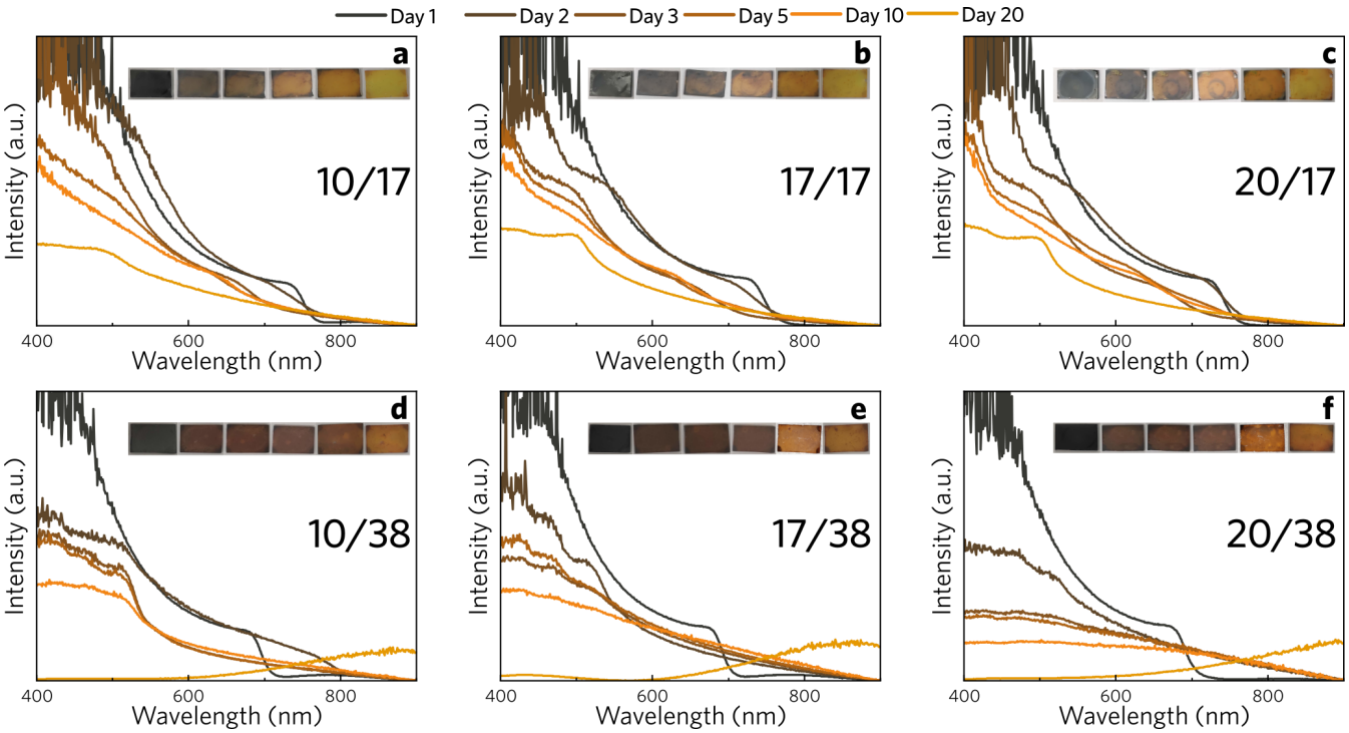

Figure 4: Uv-Vis spectra of perovskite films deposited on glass, taken during 20 days of degradation under ambient conditions – the insets show pictures of perovskite films on glass over 20 days after being prepared and stored under ambient conditions. (a - c) 17% of Br and (d - f) 38% of Br.

broad absorption at ~650nm, between 5-10 days, related to remaining of 3C phase original absorption band.[36] Sample 10/17 behaves slightly differently: there is a gradual increase in the onset until it reaches the characteristic absorption of the 2H phase (~465 nm).[36] For samples with 38%, in day 2, two distinct absorption bands appear at ~525 nm and ~465 nm, associated with 6H and 4H phases, respectively. For samples 10/38 and 17/38, these bands are present until day 10, while for sample 20/38 they last until day 3. After day 10, a new broad absorption band appears at ~850 nm, related to scattering from film irregularities.[36]

XPS can provide additional information about the surface composition of the perovskite films and, thus, help us to establish the products formed by the action of moisture and oxygen that could not be detected by XRD (i.e. amorphous phases). The XPS survey spectra for all the samples studied in this work can be found in Figures S14a to S14f. A pronounced increase in the O 1*s* (532 eV) and C 1*s* (284 eV) relative peak intensities and a decrease in the I 3d (620 eV) peak intensity after the degradation is observed. In the next paragraphs a more complete analysis will be provided based on the deconvolutions of the signals for the elements C, O, Pb, I, Cs, and Br, taken before and after degradation. The Br 3d, I 3d, Cs 3d and Pb 4f high-resolution XPS spectra of the fresh samples are shown in Figures S15 to S18. The C 1s and O 1s high-resolution XPS spectra (before and after degradation) are presented in Figures S19 and S20, respectively.

Figure 5a and 5b show the comparison of Br 3d and I 3d core-level XPS spectra, respectively, for samples containing 17% and 38% Br, after 60 of degradation at ambient conditions. We observe a wider profile in the spectra from degraded samples, which indicates the existence of more chemical components. The electrons with lower binding energies (blue) can be attributed to Br in hexagonal phases and $CsPb(I_xBr_{1-x})_3$,[49] whereas the other component (orange) can be associated with other degradation products such as $(Cs_xFA_{1-x})_4Pb(Br_yI_{1-y})_6{\cdot}2H_2O$.[50,51] For sample 10/17, the I 3d peaks are wider and a third component (green) was used to fit the results, which is related to I^- in PbI_2 (Figure 5b), in agreement with previous analyses.[52,53] Br 3d XPS for all samples presents a more significant contribution (measured by the relative integrated intensities) from the components related to the hexagonal phases (Figure 5a – blue). On the other hand, the I 3d XPS have more contribution from the component related with hydrated perovskites and other degradation products (Figure 5b – orange). It indicates that the hydrated perovskites are I-rich species, in contrast with the hexagonal phases, corroborating our *in-situ* GIWAXS and ESEM experiments. It is important to point out that, with concomitant increase in the amount of Cs in the sample, the Br 3d and I 3d XPS bands related to hydrated phases decrease for samples with 17% of Br. In contrast with the samples with 38% of Br, where the opposite behaviour occurs. This result corroborates with *in-situ* XRD results, where an increase in the stability was found for compositions with higher Cs and less Br content (Table S2).

Perovskite A-site was studied by Cs 3*d* XPS spectrum (Figure 6a and Figure S17). After degradation (Figure 6a), the Cs 3d peaks are slightly shifted to higher energies and also present a wider profile due to many components. Cs 3*d* XPS spectra were fitted with two components for all samples. One, at lower binding energy, is related to the Cs in the $CsPb(I_xBr_{1-x})_3$

phase (blue); this phase is expected to be formed as it is thermodynamically more stable in ambient conditions.[44,54,55] The other (orange) can be associated with the Cs in the hydrated perovskite species and also to CsOH.[36,50] Again, the sample 10/38 did not present the peak related to $CsPb(I_xBr_{1-x})_3$, indicating that the Cs is in $(Cs_xFA_{1-x})_4Pb(Br_yI_{1-y})_6{\cdot}2H_2O$ and other degradation products.[50]

The Pb 4f peaks broaden after several days of sample storage under ambient conditions, extending to both lower and higher binding energies Figure 6b. The main feature (blue), in the middle, is related to halide rich hydrated species, $Pb(OH)_2$, and also to the Pb cations at the dihydrate perovskite.[56–58] The component at lower energies (green) can be related to Pb(II) oxide (PbO) formation.[28] The component at higher energies (orange) can be related to $CsPb(I_xBr_{1-x})_3$ and the hexagonal phases described before. At last, we observe a small contribution at even higher binding energy, that can be assigned to lead carbonate ($PbCO_3$).[56–58] It has been reported in the literature that, in contact with water, Pb^{2+} ions in perovskite films may be converted to $Pb(OH)_2$ and, then, to PbO.[28] Also, the reaction of one of the degradation products with CO_2 and O_2, in light, can lead to the formation of $PbCO_3$.[59,60] The asymmetry towards higher energies, more evident for sample 10/17, may be composed with the contribution of lead iodide signal.[26] Sample 17/38 presents a dissonant behaviour: a wider profile for both higher and lower energies, suggesting more PbO and hydrated perovskite present in the degradation products.[28,61]

Carbon and oxygen are always present on samples exposed to the atmosphere, either because of incidental contamination or oxidation and water incorporation. The high-resolution XPS spectra for O 1s and C 1s electrons are shown in Figures S19 and S19, respectively. The C 1s component located at lower binding energy, 284.8 eV, (Figure S19) is related to C-H from *ex-situ* absorbed hydrocarbon contamination.[52] The peak area increases significantly after degradation. At 286 and 288 eV contributions from electrons of C-N bond[62,63] and from the conjugated N-C=N carbon of formamidinium ion can be found.[62,63] At last, the signal at ~289 eV is attributed to C=O/C-O.[26,61,64] The features in the O 1s XPS spectrum (Figure S20), at 532.2 and 533.5 eV confirm the C=O/C-O bonds observed in the C 1s spectrum. The component at higher energy (533.5 eV) is derived from metal hydroxides, that can be lead(II) hydroxide ($Pb(OH)_2$),[28,65] and the other (532.2 eV), originated from C-O/C=O bond in $PbCO_3$, overlapping with features related to water in the hydrated perovskite lattice, which explains, also, the size of this Gaussian componnent.[28,66] The component at 530.5 eV in the O *1s* XPS spectrum is attributed to PbO, corroborating the Pb 4f XPS results.[28,66] We observe, further, other small feature at about 536 eV, related to water absorbed by the perovskite film.

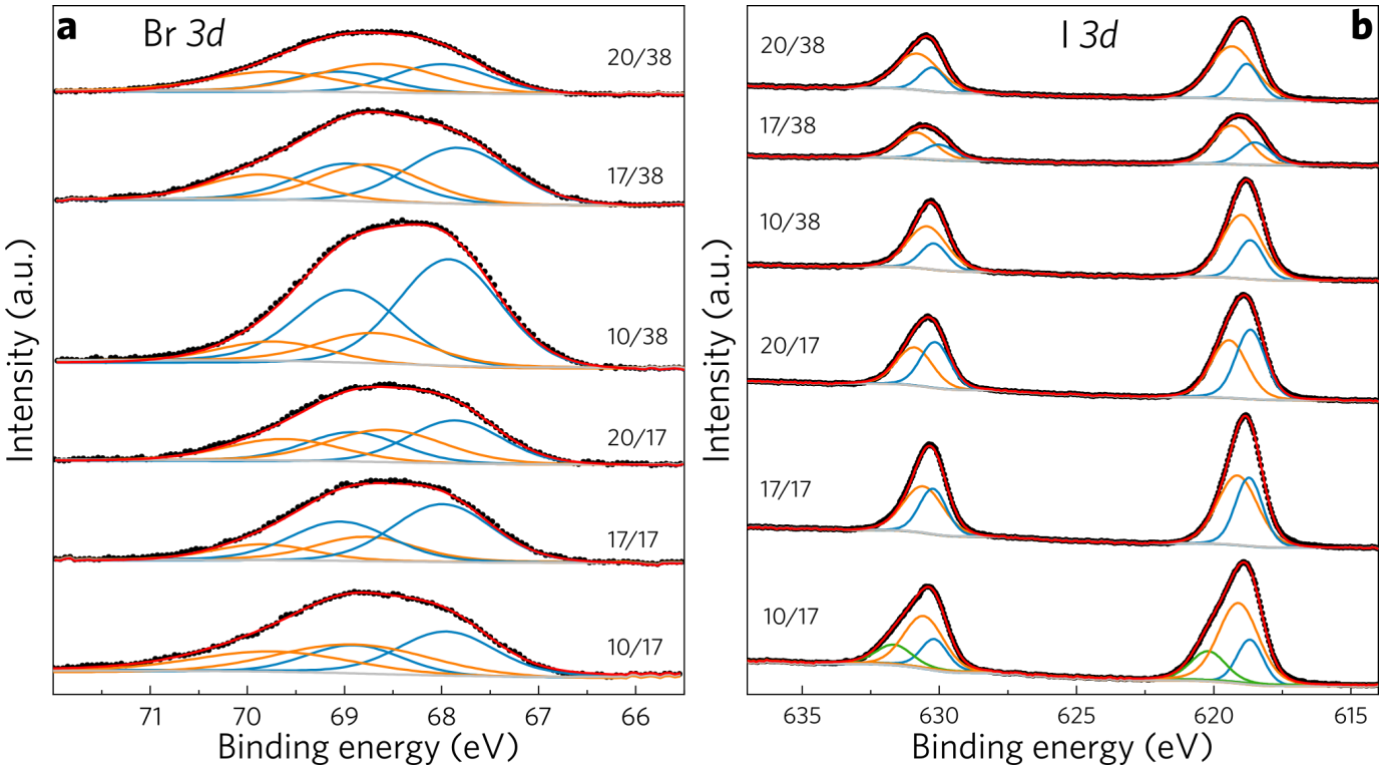

Figure 5: High resolution XPS analysis. (a) After degradation high resolution XPS Br 3d core level spectra of all samples - deconvolution peaks are attributed to hexagonal phases, $CsPb(I_xBr_{1-x})_3$ (blue), $(Cs_xFA_{1-x})_4Pb(Br_yI_{1-y})_6{\cdot}2H_2O$ and other degradation products (orange); (b) After degradation high resolution XPS I 3d core-level spectra of all samples - deconvolution peaks are attributed to hexagonal phases, $CsPb(I_xBr_{1-x})_3$ (blue), $(Cs_xFA_{1-x})_4Pb(Br_yI_{1-y})_6{\cdot}2H_2O$ (orange), and PbI_2 (green). The ratios between the deconvoluted areas are presented in Table S2.

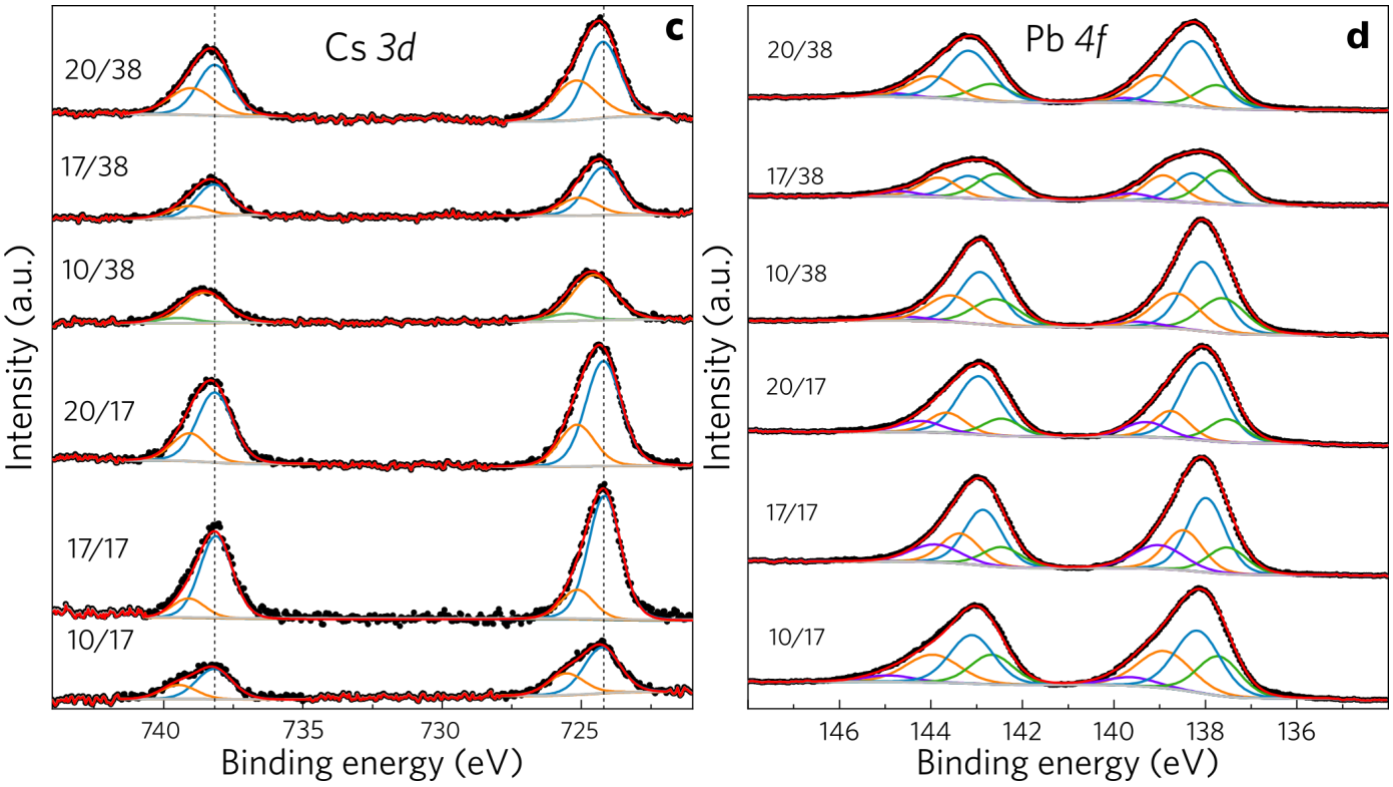

Figure 2: High resolution XPS analysis. (a) After degradation high resolution XPS Cs 3d core-level spectra of all samples - deconvolution peaks are attributed to Cs electrons in $(Cs_xFA_{1-x})_4Pb(Br_yI_{1-y})_6{\cdot}2H_2O$ and, also, CsOH (orange), in $CsPb(I_xBr_{1-x})_3$ phases (blue) and, for sample 10/38, to Cs in other degradation sub products such as CsX and CsOH (green); (b) High resolution XPS Pb *4f* core level spectra of samples, after degradation - The deconvolutions are attributed to $(Cs_xFA_{1-x})_4Pb(Br_yI_{1-y})_6{\cdot}2H_2O$, hexagonal phases, $Pb(OH)_2$ (blue), $PbCO_3$ (orange), $CsPb(I_xBr_{1-x})_3$ (purple), and PbO (green).

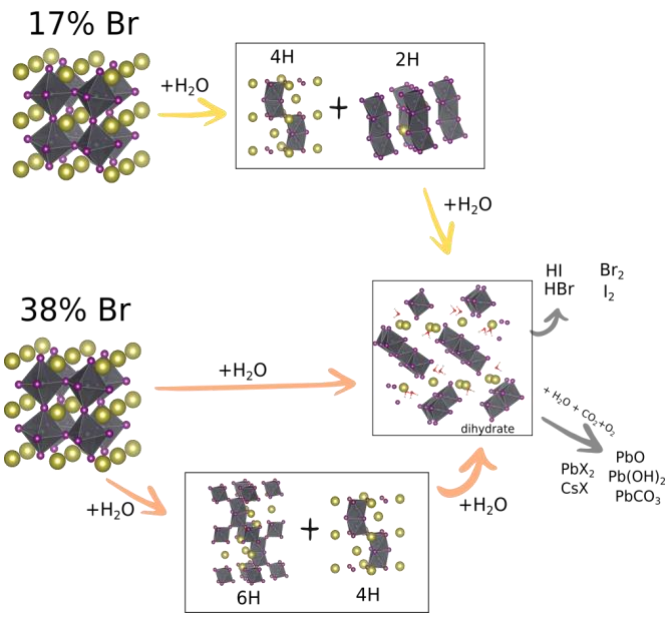

Figure 3: Scheme of the possible perovskite degradation pathways, depending on the initial composition. We note that, with less amount of Br, the perovskite passes through 4H and 2H phases before forming the hydrated perovskite. On the other hand, the perovskites with higher Br content can form both the phase 6H and the hydrated perovskite simultaneously.

S21b) suggests a loss of iodine and bromine during the degradation process. Analysing the results summarized in Table S3, the ratio [Br + I]/Pb decreases almost to half of the initial value. This indicates that part of the halides is lost in the degradation processes. The ratio ([Br + I]/Pb) value is much lower than the expected value considering only the hydration products. This corroborates our findings of other degradation products as PbO, $Pb(OH)_2$ and $PbCO_3$. Similar behaviour is found for (Br3d+I3d)/Cs3d area ratio (Table S3). Here, we observe a decrease in the Cs content almost to the same extent of the halides (Figures S21c and S21d). This can be associated with the higher mobility of Cs and halides in water.[67,68]

In summary, for perovskites containing 17% of Br, the degradation mechanism passes, necessarily, through 4H and 2H hexagonal phases. On the other hand, the perovskites with 38% of Br pass simultaneously through hexagonal phases and hydrated structures. When the hydrated perovskites are then formed, other reactions take place, due to the higher amount of water in these structures. Consequently, different degradation products are formed. Evolution of HI and HBr are expected to shift the reaction equilibrium in the direction of the products, promoting the formation of metal hydroxides ($Pb(OH)_2$ and CsOH), oxides (PbO), and carbonates ($PbCO_3$). The possible reaction mechanisms and the products formed are depicted in (Figure 7).

Conclusions

In this work the degradation mechanisms of mixed-cation perovskite films with different stoichiometries ($Cs_xFA_{1-x}Pb(Br_yI_{1-y})_3$) were investigated by *in-situ*, structural and surface techniques. Our study presents new findings on how mixed-halide and mixed-cation perovskites can degrade when exposed to ambient conditions. We tracked the initial stages of perovskite degradation using *in-situ* ESEM and GIWAXS. The compositions with 17% of Br begin to degrade with the formation of hexagonal phases (2H and 4H) and, then, hydration starts to occur. For perovskites with 38% of Br, the formation of 6H hexagonal phase and hydration occur almost simultaneously due to the heterogeneity of the Br and I distribution in the film. *In-situ* FEG-ESEM images obtained in a chamber at 75% of RH was obtained for the first time to track visually the beginning of degradation. It was possible to visualize that the hexagonal phases start to appear at the "valleys" of the wrinkled morphology presented by these films, likely related to smaller grain size in these parts of the film. After the initial stages, the reactions lead to the formation of other products (hydroxides, oxides and carbonates), due to the evolution of halide gases, independent of the initial composition.

Additionally, we observed that higher fractions of Cs increase the stability, while higher Br fraction has the opposite effect and is detrimental to stability. Our findings provide a guide for selecting the best compositions, type of protective layers (e.g. when applying these films as top layer in tandem solar cells) and postconditioning procedures for perovskite thin films.

Another highly important aspect of this work is the recycling of devices that are no longer functional. Given the fact that many companies have started in the PSCs business, it is of critical relevance the adequate management/recycling of these devices after usage.[69] And for the correct disposal, our investigation provides detailed information about the final products as a consequence of the complete degradation of multicomponent perovskites.

Conflicts of interest

There are no conflicts to declare.

Acknowledgements

The authors thank the support from the Laboratorio Nacional de Luz Sincrotron (LNLS), XRD2 facility. The authors are grateful to Dr. Renato V. Gonçalves for kindly providing access to the XPS instrument. The authors are grateful to Anderson Bordin and Antonio Malfatti Gasperini for the great help with reciprocal lattice plots and analysis of GIWAXS data. Authors thank to José Carlos Germino and Raphael Fernando Moral for their great help in the discussions and revision of the manuscript. A.F.N., P.E.M., M. A. M. Jr and R. S gratefully acknowledge support from FAPESP (the Sao Paulo Research Foundation, Process 2017/11986-5) and Shell and the strategic importance of the support given by ANP (Brazil's National Oil, Natural Gas and Biofuels Agency) through the R&D levy regulation. E.M.T. acknowledges CNPq (150043/2018-0). P.E.M and A.F.N. also acknowledge the CNPq and CAPES. Use of the Stanford Synchrotron Radiation Lightsource, SLAC National Accelerator Laboratory, is supported by the U.S. Department of Energy, Office of Science, Office of Basic Energy Sciences under Contract No. DE-AC02-76SF00515.

Notes and references

1 R. Fan, Y. Huang, L. Wang, L. Li, G. Zheng and H. Zhou, *Adv. Energy Mater.*, 2016, **6**, 1600460.

2 N. J. Jeon, J. H. Noh, Y. C. Kim, W. S. Yang, S. Ryu and S. Il Seok, *Nat. Mater.*, 2014, **13**, 897–903.

3 R. Szostak, J. A. P. Castro, A. S. Marques and A. F. Nogueira, *J. Photonics Energy*, 2017, **7**, 022002.

4 C. Zuo, H. J. Bolink, H. Han, J. Huang, D. Cahen and L. Ding, *Adv. Sci.*, 2016, **3**, 1500324.

5 H. S. Jung and N.-G. Park, *Small*, 2015, **11**, 10–25.

6 A. Kojima, K. Teshima, Y. Shirai and T. Miyasaka, *J. Am. Chem. Soc.*, 2009, **131**, 6050–6051.

7 J. Huang, Y. Yuan, Y. Shao and Y. Yan, *Nat. Rev. Mater.*, 2017, **2**, 17042.

8 NREL Best Research-Cell Efficiency Chart, https://www.nrel.gov/pv/cell-efficiency.html, (accessed 6 March 2020).

9 H. J. Snaith and P. Hacke, *Nat. Energy*, 2018, **3**, 459–465.

10 A. K. Jena, A. Kulkarni and T. Miyasaka, *Chem. Rev.*, 2019, **119**, 3036–3103.

11 Y. Rong, Y. Ming, W. Ji, D. Li, A. Mei, Y. Hu and H. Han, *J. Phys. Chem. Lett.*, 2018, **9**, 2707–2713.

12 K. A. Bush, A. F. Palmstrom, Z. J. Yu, M. Boccard, R. Cheacharoen, J. P. Mailoa, D. P. McMeekin, R. L. Z. Hoye, C. D. Bailie, T. Leijtens, I. M. Peters, M. C. Minichetti, N. Rolston, R. Prasanna, S. Sofia, D. Harwood, W. Ma, F. Moghadam, H. J. Snaith, T. Buonassisi, Z. C. Holman, S. F. Bent and M. D. McGehee, *Nat. Energy*, 2017, **2**, 17009.

13 G. E. Eperon, T. Leijtens, K. A. Bush, R. Prasanna, T. Green, J. T.-W. Wang, D. P. McMeekin, G. Volonakis, R. L. Milot, R. May, A. Palmstrom, D. J. Slotcavage, R. A. Belisle, J. B. Patel, E. S. Parrott, R. J. Sutton, W. Ma, F. Moghadam, B. Conings, A. Babayigit, H.-G. Boyen, S. Bent, F. Giustino, L. M. Herz, M. B. Johnston, M. D. McGehee and H. J. Snaith, *Science*, 2016, **354**, 861–865.

14 C. D. Bailie, M. G. Christoforo, J. P. Mailoa, A. R. Bowring, E. L. Unger, W. H. Nguyen, J. Burschka, N. Pellet, J. Z. Lee, M. Grätzel, R. Noufi, T. Buonassisi, A. Salleo and M. D. McGehee, *Energy Environ. Sci.*, 2015, **8**, 956–963.

15 F. Sahli, J. Werner, B. A. Kamino, M. Bräuninger, R. Monnard, B. Paviet-Salomon, L. Barraud, L. Ding, J. J. Diaz Leon, D. Sacchetto, G. Cattaneo, M. Despeisse, M. Boccard, S. Nicolay, Q. Jeangros, B. Niesen and C. Ballif, *Nat. Mater.*, 2018, **17**, 820–826.

16 D. Zhao, Y. Yu, C. Wang, W. Liao, N. Shrestha, C. R. Grice, A. J. Cimaroli, L. Guan, R. J. Ellingson, K. Zhu, X. Zhao, R.-G. Xiong and Y. Yan, *Nat. Energy*, 2017, **2**, 17018.

17 T. Duong, Y. Wu, H. Shen, J. Peng, X. Fu, D. Jacobs, E.-C.

Wang, T. C. Kho, K. C. Fong, M. Stocks, E. Franklin, A. Blakers, N. Zin, K. McIntosh, W. Li, Y.-B. Cheng, T. P. White, K. Weber and K. Catchpole, *Adv. Energy Mater.*, 2017, **7**, 1700228.

18 T. Jesper Jacobsson, J.-P. Correa-Baena, M. Pazoki, M. Saliba, K. Schenk, M. Grätzel and A. Hagfeldt, *Energy Environ. Sci.*, 2016, **9**, 1706–1724.

19 K. A. Bush, K. Frohna, R. Prasanna, R. E. Beal, T. Leijtens, S. A. Swifter and M. D. McGehee, *ACS Energy Lett.*, 2018, **3**, 428–435.

20 G. Grancini, C. Roldán-Carmona, I. Zimmermann, E. Mosconi, X. Lee, D. Martineau, S. Narbey, F. Oswald, F. De Angelis, M. Graetzel and M. K. Nazeeruddin, *Nat. Commun.*, , DOI:10.1038/ncomms15684.

21 S. N. Habisreutinger, T. Leijtens, G. E. Eperon, S. D. Stranks, R. J. Nicholas and H. J. Snaith, *Nano Lett.*, 2014, **14**, 5561–5568.

22 L. Zheng, Y.-H. Chung, Y. Ma, L. Zhang, L. Xiao, Z. Chen, S. Wang, B. Qu and Q. Gong, *Chem. Commun.*, 2014, **50**, 11196–11199.

23 F. Villani, P. Vacca, G. Nenna, O. Valentino, G. Burrasca, T. Fasolino, C. Minarini and D. Della Sala, *J. Phys. Chem. C*, 2009, **113**, 13398–13402.

24 Y. Wang, M. I. Dar, L. K. Ono, T. Zhang, M. Kan, Y. Li, L. Zhang, X. Wang, Y. Yang, X. Gao, Y. Qi, M. Grätzel and Y. Zhao, *Science*, 2019, **365**, 591–595.

25 S. Wozny, M. Yang, A. M. Nardes, C. C. Mercado, S. Ferrere, M. O. Reese, W. Zhou and K. Zhu, *Chem. Mater.*, 2015, **27**, 4814–4820.

26 J. Chun-Ren Ke, A. S. Walton, D. J. Lewis, A. Tedstone, P. O'Brien, A. G. Thomas and W. R. Flavell, *Chem. Commun.*, 2017, **53**, 5231–5234.

27 B. Hailegnaw, S. Kirmayer, E. Edri, G. Hodes and D. Cahen, *J. Phys. Chem. Lett.*, 2015, **6**, 1543–1547.

28 W. Huang, J. S. Manser, P. V. Kamat and S. Ptasinska, *Chem. Mater.*, 2016, **28**, 303–311.

29 N. Aristidou, I. Sanchez-Molina, T. Chotchuangchutchaval, M. Brown, L. Martinez, T. Rath and S. A. Haque, *Angew. Chemie Int. Ed.*, 2015, **54**, 8208–8212.

30 J. Huang, S. Tan, P. D. Lund and H. Zhou, *Energy Environ. Sci.*, 2017, 10, 2284–2311.

31 J. M. Howard, E. M. Tennyson, S. Barik, R. Szostak, E. Waks, M. F. Toney, A. F. Nogueira, B. R. A. Neves and M. S. Leite, *J. Phys. Chem. Lett.*, 2018, **9**, 3463–3469.

32 Y. Hu, M. F. Aygüler, M. L. Petrus, T. Bein and P. Docampo, *ACS Energy Lett.*, 2017, **2**, 2212–2218.

33 N. J. Jeon, J. H. Noh, Y. C. Kim, W. S. Yang, S. Ryu and S. Il Seok, *Nat. Mater.*, 2014, **13**, 897–903.

34 H. X. Dang, K. Wang, M. Ghasemi, M.-C. Tang, M. De Bastiani, E. Aydin, E. Dauzon, D. Barrit, J. Peng, D.-M. Smilgies, S. De Wolf and A. Amassian, *Joule*, 2019, **3**, 1746–1764.

35 L. S. Ramsdell, *Am. Mineral.*, 1947, **32**, 64–82.

36 P. Gratia, I. Zimmermann, P. Schouwink, J.-H. Yum, J.-N. Audinot, K. Sivula, T. Wirtz and M. K. Nazeeruddin, *ACS Energy Lett.*, 2017, **2**, 2686–2693.

37 P. Gratia, I. Zimmermann, P. Schouwink, J. H. Yum, J. N. Audinot, K. Sivula, T. Wirtz and M. K. Nazeeruddin, *ACS Energy Lett.*, 2017, **2**, 2686–2693.

38 M. I. Saidaminov, K. Williams, M. Wei, A. Johnston, R. Quintero-Bermudez, M. Vafaie, J. M. Pina, A. H. Proppe, Y. Hou, G. Walters, S. O. Kelley, W. A. Tisdale and E. H. Sargent, *Nat. Mater.*, 2020, **19**, 1–7.

39 M. Saliba, T. Matsui, J.-Y. Seo, K. Domanski, J.-P. Correa-Baena, M. K. Nazeeruddin, S. M. Zakeeruddin, W. Tress, A. Abate, A. Hagfeldt and M. Grätzel, *Energy Environ. Sci.*, 2016, **9**, 1989–1997.

40 Z. Wang, Y. Zhou, S. Pang, Z. Xiao, J. Zhang, W. Chai, H. Xu, Z. Liu, N. P. Padture and G. Cui, *Chem. Mater.*, 2015, **27**, 7149–7155.

41 A. F. Xu, R. T. Wang, L. W. Yang, V. Jarvis, J. F. Britten and G. Xu, *Chem. Commun.*, 2019, **55**, 3251–3253.

42 F. Hao, C. C. Stoumpos, Z. Liu, R. P. H. Chang and M. G. Kanatzidis, *J. Am. Chem. Soc.*, 2014, **136**, 16411–16419.

43 A. M. A. Leguy, Y. Hu, M. Campoy-Quiles, M. I. Alonso, O. J. Weber, P. Azarhoosh, M. Van Schilfgaarde, M. T. Weller, T. Bein, J. Nelson, P. Docampo and P. R. F. Barnes, *Chem. Mater.*, 2015, **27**, 3397–3407.

44 B. Zhao, S.-F. Jin, S. Huang, N. Liu, J.-Y. Ma, D.-J. Xue, Q. Han, J. Ding, Q.-Q. Ge, Y. Feng and J.-S. Hu, *J. Am. Chem. Soc.*, 2018, **140**, 11716–11725.

45 R. Szostak, P. E. Marchezi, A. dos S. Marques, J. C. da Silva, M. S. de Holanda, M. M. Soares, H. C. N. Tolentino and A. F. Nogueira, *Sustain. Energy Fuels*, 2019, **3**, 2287–2297.

46 K. A. Bush, N. Rolston, A. Gold-Parker, S. Manzoor, J. Hausele, Z. J. Yu, J. A. Raiford, R. Cheacharoen, Z. C. Holman, M. F. Toney, R. H. Dauskardt and M. D. McGehee, *ACS Energy Lett.*, 2018, **3**, 1225–1232.

47 J. Schlipf, L. Bießmann, L. Oesinghaus, E. Berger, E. Metwalli, J. A. Lercher, L. Porcar and P. Müller-Buschbaum, *J. Phys. Chem. Lett.*, 2018, **9**, 2015–2021.

48 K. A. Bush, K. Frohna, R. Prasanna, R. E. Beal, T. Leijtens, S. A. Swifter and M. D. McGehee, *ACS Energy Lett.*, 2018, **3**, 428–435.

49 Z. Li, J. Xu, S. Zhou, B. Zhang, X. Liu, S. Dai and J. Yao, *ACS Appl. Mater. Interfaces*, 2018, 10, 38183–38192.

50 J. Liang, P. Zhao, C. Wang, Y. Wang, Y. Hu, G. Zhu, L. Ma, J. Liu and Z. Jin, *J. Am. Chem. Soc.*, 2017, **139**, 14009–14012.

51 Z. Li, J. Xu, S. Zhou, B. Zhang, X. Liu, S. Dai and J. Yao, *ACS Appl. Mater. Interfaces*, 2018, **10**, 38183–38192.

52 L. Liu, J. A. McLeod, R. Wang, P. Shen and S. Duhm, *Appl. Phys. Lett.*, 2015, **107**, 061904.

53 C. Das, M. Wussler, T. Hellmann, T. Mayer and W. Jaegermann, *Phys. Chem. Chem. Phys.*, 2018, **20**, 17180–17187.

54 J. A. Steele, H. Jin, I. Dovgaliuk, R. F. Berger, T. Braeckevelt, H. Yuan, C. Martin, E. Solano, K. Lejaeghere, S. M. J. Rogge, C. Notebaert, W. Vandezande, K. P. F. Janssen, B. Goderis, E. Debroye, Y. K. Wang, Y. Dong, D. Ma, M. Saidaminov, H. Tan, Z. Lu, V. Dyadkin, D. Chernyshov, V. Van Speybroeck, E. H. Sargent, J. Hofkens and M. B. J. Roeffaers, *Science*, 2019, **365**, 679–684.

55 T. Burwig, W. Fränzel and P. Pistor, *J. Phys. Chem. Lett.*, 2018, **9**, 4808–4813.

56 K. Lin, J. Xing, L. N. Quan, F. P. G. de Arquer, X. Gong, J. Lu, L. Xie, W. Zhao, D. Zhang, C. Yan, W. Li, X. Liu, Y. Lu, J. Kirman, E. H. Sargent, Q. Xiong and Z. Wei, *Nature*, 2018, **562**, 245–248.

57 T.-W. Ng, C.-Y. Chan, M.-F. Lo, Z. Q. Guan and C.-S. Lee, *J. Mater. Chem. A*, 2015, **3**, 9081–9085.

58 B. Philippe, B.-W. Park, R. Lindblad, J. Oscarsson, S. Ahmadi, E. M. J. Johansson and H. Rensmo, *Chem. Mater.*, 2015, **27**, 1720–1731.

59 M. Acik, I. K. Park, R. E. Koritala, G. Lee and R. A. Rosenberg, *J. Mater. Chem. A*, 2018, **6**, 1423–1442.

60 S. Olthof and K. Meerholz, *Sci. Rep.*, 2017, **7**, 40267.

61 C. Rocks, V. Svrcek, P. Maguire and D. Mariotti, *J. Mater. Chem. C*, 2017, **5**, 902–916.

62 B. Philippe, M. Saliba, J.-P. Correa-Baena, U. B. Cappel, S.-H. Turren-Cruz, M. Grätzel, A. Hagfeldt and H. Rensmo, *Chem. Mater.*, 2017, **29**, 3589–3596.

63 J. Yang, X. Liu, Y. Zhang, X. Zheng, X. He, H. Wang, F. Yue, S. Braun, J. Chen, J. Xu, Y. Li, Y. Jin, J. Tang, C. Duan, M. Fahlman and Q. Bao, *Nano Energy*, 2018, **54**, 218–226.

64 P. Chen, Y. Bai, S. Wang, M. Lyu, J. H. Yun and L. Wang, *Adv. Funct. Mater.*, 2018, **28**, 1–10.

65 P. Nowak and K. Laajalehto, *Physicochem. Probl. Miner. Process.*, 2007, **41**, 107–116.

66 D. J. Payne, R. G. Egdell, D. S. L. Law, P.-A. Glans, T. Learmonth, K. E. Smith, J. Guo, A. Walsh and G. W. Watson, *J. Mater. Chem.*, 2007, **17**, 267–277.

67 S. H. Lee and J. C. Rasaiah, *J. Phys. Chem.*, 1996, **100**, 1420–1425.

68 N. T. P. Hartono, S. Sun, M. C. Gélvez-Rueda, P. J. Pierone, M. P. Erodici, J. Yoo, F. Wei, M. Bawendi, F. C. Grozema, M. Sher, T. Buonassisi and J.-P. Correa-Baena, *J. Mater. Chem. A*, 2019, **7**, 23949–23957.

69 A. Extance, *Nature*, 2019, **570**, 429–432.

Table of contents entry

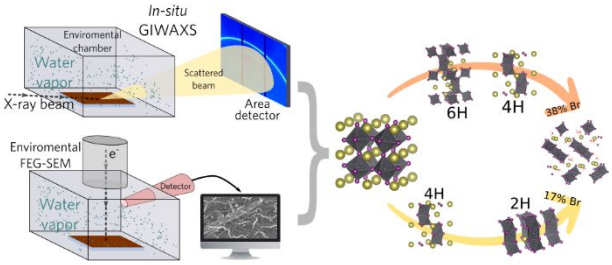

With *in-situ* ESEM and GIWAXS we saw that the degradation passess through hexagonal polytypes and are dependent on the composition.